Journal of Magnetic Resonance 303 (2019) 17–27

Contents lists available at ScienceDirect

Journal of Magnetic Resonance

journal homepage: www.elsevier.com/locate/jmr

^{1}H high field electron-nuclear double resonance spectroscopy at 263 GHz/9.4 T

Igor Tkach [a,*], Isabel Bejenke [a], Fabian Hecker [a], Annemarie Kehl [a,b], Müge Kasanmascheff [a,1], Igor Gromov [c], Ion Prisecaru [c], Peter Höfer [c], Markus Hiller [a], Marina Bennati [a,b,*]

[a] Research Group EPR Spectroscopy, Max Planck Institute for Biophysical Chemistry, Am Fassberg 11, 37077 Göttingen, Germany
[b] Department of Chemistry, Georg-August University of Göttingen, Tammannstr. 2, Göttingen, Germany
[c] Bruker Biospin GmbH, Silberstreifen 4, 76287 Rheinstetten, Germany

ARTICLE INFO

Article history:
Received 3 December 2018
Revised 18 March 2019
Accepted 2 April 2019
Available online 3 April 2019

Keywords:
High field ENDOR and EPR
263 GHz ENDOR setup
263 GHz ENDOR resonator, high frequency
Hyperfine spectroscopy
Nuclear spins
Tyrosyl radicals

ABSTRACT

We present and discuss the performance of ^{1}H electron-nuclear double resonance (ENDOR) at 263 GHz/9.4 T by employing a prototype, commercial quasi optical spectrometer. Basic instrumental features of the setup are described alongside a comprehensive characterization of the new ENDOR probe head design. The performance of three different ENDOR pulse sequences (Davies, Mims and CP-ENDOR) is evaluated using the ^{1}H BDPA radical. A key feature of 263 GHz spectroscopy – the increase in orientation selectivity in comparison with 94 GHz experiments – is discussed in detail. For this purpose, the resolution of ^{1}H ENDOR spectra at 263 GHz is verified using a representative protein sample containing approximately 15 picomoles of a tyrosyl radical. Davies ENDOR spectra recorded at 5 K reveal previously obscured spectral features, which are interpreted by spectral simulations aided by DFT calculations. Our analysis shows that seven internal proton couplings are detectable for this specific radical if sufficient orientation selectivity is achieved. The results prove the fidelity of 263 GHz experiments in reporting orientation-selected ^{1}H ENDOR spectra and demonstrate that new significant information can be uncovered in complex molecular systems, owing to the enhanced resolution combined with high absolute sensitivity and no compromise in acquisition time.

1. Introduction

Electron-nuclear double resonance (ENDOR) defines a group of EPR-based double frequency methods to detect magnetic nuclei in the vicinity of paramagnetic centers [1–6]. It enables to detect hyperfine (hf) interactions in the range from hundreds of MHz down to tens of kHz [7] that are often not resolved in an inhomogeneously broadened EPR line and also not easily accessible by paramagnetic NMR [8]. ENDOR was initially introduced as a continuous wave (cw) technique [6,9,10], which was later extended to several pulse methods. Basic ENDOR pulse sequences, such as Mims [1] and Davies [2], consist of series of microwaves (mw) pulses to drive and detect EPR transitions, while a radio frequency (RF) pulse is applied to excite nuclear transitions. The detected signal is a change of the EPR line intensity monitored during an RF frequency sweep. In principle, the experiment can be performed at any magnetic field, however the optimal field range depends on a paramagnetic system in study.

At high magnetic fields ($\gtrsim$3 T), several advantages arise from ENDOR [11–14]. The detection sensitivity of high-frequency/high-field EPR spectrometers is largely increased, leading to the capability of working with small sample volumes ($\lesssim$1 μL) at μM sample concentrations. This is a crucial advantage for protein or nucleic acid research, where the available sample amount is usually limited. Higher magnetic fields also lead to a higher nuclear Zeeman resolution for low-γ nuclei as well as to 'first order' type hyperfine spectra [15–17], which are much easier to simulate and interpret. The most characteristic feature in high-frequency/high-field (HF) ENDOR is that a standard rectangular microwave pulse excites merely a small fraction of the EPR spectrum, thus covering only a few molecular orientations in a sample randomly oriented with respect to the external magnetic field. This can be utilized to perform so-called orientation selection, from which not only distance information but also hf tensor orientations with

* Corresponding authors at: Research Group EPR Spectroscopy, Max Planck Institute for Biophysical Chemistry, Am Fassberg 11, 37077 Göttingen, Germany (I. Tkach, M. Bennati).
E-mail addresses: igor.tkach@mpibpc.mpg.de (I. Tkach), mbennat@gwdg.de (M. Bennati).
[1] Present address: Department of Chemistry and Chemical Biology, Technical University of Dortmund, Otto-Hahn-Str. 6, 44227 Dortmund, Germany.

https://doi.org/10.1016/j.jmr.2019.04.001
1090-7807/

respect to the molecular axes of the paramagnetic center can be extracted. For all these reasons, in the last decade HF ENDOR has been widely applied to elucidate detailed structural arrangements of ligands surrounding paramagnetic centers [18–26].

However, despite the fact that the first HF ENDOR spectrometers operating at 94 GHz were built more than two decades ago [27–29] and ENDOR at 275 GHz [13] was introduced more than a decade ago, ENDOR studies in the frequency range $\gtrsim$200 GHz are scarce. In this paper, we demonstrate some attractive features of 263 GHz ENDOR, *i.e.* the increased spectral resolution combined with the intrinsic absolute sensitivity, which can be particularly useful to disentangle complex ^{1}H ENDOR spectra contributed by several nuclei. We employ our quasi-optical EPR/ENDOR spectrometer (Bruker BioSpin) operating at 263 GHz (9.4 T) and describe a new probe head design in context of its ENDOR performance using the protonated 1,3-bis(diphenylene)-2-phenyl-allyl (BDPA) radical as a model system. In a second step, we present a comparison of 94 and 263 GHz HF ENDOR spectra on a protein radical, the native tyrosyl radical Y_{122}· from *E. coli* ribonucleotide reductase (RNR). Experiments and analysis consistently show that new spectral features become visible at 263 GHz, accessing new information content. The availability of increased spectral resolution in 263 GHz ^{1}H ENDOR combined with the intrinsically high absolute sensitivity and no compromise in spectral acquisition time will potentially expand the application of ENDOR spectroscopy to studies of more complex biological systems under real sample conditions.

2. Methods

Samples: Protonated BDPA (1,3-bis(diphenylene)-2-phenyl-allyl) radical was dispersed in a protonated polystyrene matrix (0.1% w/w) and loaded into 0.2-mm-ID (inner diameter) quartz capillaries with a filling volume of about 30÷50 nL. Wild-type (wt) RNR-β_2 protein subunit was prepared in H_2O buffer consisting of 50 mM HEPES, 15 mM $MgSO_4$ and 1 mM EDTA adjusted to pH = 8.0. The estimated concentrations of the Y_{122}· radical in solution were around 300 μM and 200 μM for measurements at 263 GHz and 94 GHz, respectively. Protein solutions were loaded in capillary tubes (Vitrocom CV2033S/Q with OD (outer diameter) = 0.33 mm and ID = 0.2 mm for 263 GHz; and OD = 0.87 mm and ID = 0.70 mm for 94 GHz), and subsequently quickly frozen in liquid N_2. For 263 GHz, sample capillaries were inserted into the precooled resonator immersed in a liquid N_2 bath. The cold probe head was transferred into the cryostat, precooled to ≈ 100 K. In contrast, sample capillaries for 94 GHz were inserted into the resonator, precooled to ≈ 80 K directly inside the cryostat.

94 GHz pulsed EPR/ENDOR: Spectra were recorded on a Bruker E680 W-band spectrometer equipped with a new 2 W microwave amplifier (Quinstar), leading to typical π pulse lengths of ≈ 20 ns. Samples for 94 GHz spectroscopy contained typical volumes of ∼2 μL. RF pulses were amplified with a 250 W RF-amplifier (250A250A, Amplifier Research). Typical ^{1}H RF pulse lengths at this frequency were 20 μs and 60 μs for "hard" and "soft" RF excitation, respectively.

Simulations of ENDOR Spectra. ENDOR spectra were simulated using a MATLAB routine developed in house [30], which computes EPR spectra, orientation selection and ENDOR frequencies based on a first order Hamiltonian (high field approximation) for the hyperfine interactions [16]. For the ENDOR spectra, ENDOR resonances were convolved with a Lorentzian line shape. Powder averaging was performed with 0.1° and 0.25° increments in the range of $0 \div \pi/2$ and $0 \div \pi$ for θ and φ polar and azimuthal angles, respectively. The "hole burning"-effect from the inversion pulse in the Davies sequence is included by multiplying the calculated ENDOR powder pattern with an envelope function given in the text (Eq. (2)). The ENDOR simulations were reproduced with the *EasySpin* "salt"-routine using approximations of the first order perturbation theory [31], and a Gaussian linewidth for a single ENDOR transition, whereas the number of knots was set to 200. To take into account different notations for tensor transformations, *i.e.* "hf-tensor to molecular frame" as in the home-written algorithm vs. "molecular frame to hf-tensor" as in *EasySpin*, the *EasySpin* spectra were simulated with the inverted order and the sign of the three Euler angles (-γ, -β, -α instead of α, β, γ). In both programs, positive angles are clockwise rotations when viewed along the rotation axis, *i.e.* following the right-hand rule.

Simulations of EPR spectra. Spectral simulations were carried out using the *'pepper'* routine in *EasySpin*. Full matrix diagonalization and 3° increments in powder average were employed. The isotropic linewidth (*'lw'*) for the simulation was chosen to be a Gaussian with FWHM of 2.5 G. The parameters for *g* strain were then optimized in order to best reproduce the spectral features. Hyperfine interactions with all 7 nuclei given in Table 1 were included in the simulations. The signs and the order of the Euler angles were inverted as compared to those in Table 1 to match the *EasySpin* convention, as explained in the above paragraph.

DFT calculations. All calculations were performed with ORCA 4.0.1.2 [32] employing the B3LYP functional [33–36] in

Table 1
Hf parameters used in ENDOR spectra simulations for Y_{122}· andcomparison with DFT predicted tensor values and Euler angles using the conformation for the radical structure from Ref. [44]. Bold values are from Ref. [30], Italic values for ^{1}H-Cβ1 are from the EPR simulation and consistent with Ref. [65], regular-font values are from the ENDOR simulation. For the H-Cβ1 coupling, the hf-parameters were used only to compute the orientation selection and to simulate the EPR spectrum. One representative spectrum for the ^{1}H-Cβ1 is displayed in Fig. S13. The second row of DFT predicted values for C_3/C_5 indicate a non-equivalent set. However, we note that this non-equivalency is within the error of the DFT prediction and was not found either in this or in any previous data analysis [30,71]. A simulation with the non-equivalent set predicted by the DFT is displayed in Fig. S16. For both ENDOR and DFT simulations, Euler angles α, ß and γ are defined by z, y′, z″ – convention and refer to rotations from the hyperfine tensor frame into the *g* tensor frame. Positive angles are clockwise rotations when viewed along the rotation axis, *i.e.* following the right-hand rule. Numbering of the atoms is given in Fig. 5A. Uncertainty in the simulated hf values is up to 10% and considers also uncertainty in the magnetic field value due to hysteresis. Uncertainty in the DFT calculated values is up to 20%.

	Simulated hfcs from ENDOR						DFT predicted hfcs					
	A_x (MHz)	A_y (MHz)	A_z (MHz)	α	β	γ	A_x (MHz)	A_y (MHz)	A_z (MHz)	α	β	γ
^{1}H-Cβ1	*59*	*55*	*56*	–	–	–	52.5	47.4	46.0	46	59	63
^{1}H-Cβ2	8	−1	−1	7	−4	−70	5.2	−0.6	−0.1	7	−4	−70
	−2.1	**6.2**	**−1**									
^{1}H-Cα	1.2	−1.0	−4.1	0	20	−60	1.3	−2.1	−2.9	0	19	−58
	–	**–**	**–**									
C_3/C_5 ring protons	−27.2	−7.9	−19.8	25/155	0	0	−28	−6	−20	25	0	0
	−26.4	**−8.1**	**−19.3**				−25	−6	−18	−30	0	0
C_2/C_6 ring protons	4.9	7.7	1.7	−25/	0	0	6	10	3	−44	0	0
	4.9	**7.7**	**1.9**	−155						44	0	0

combination with the def2-TZVPP basis sets [37] for all atoms and the RIJCOSX approximation [38,39]. The geometry of the model system was optimized employing dispersion correction (d3bj) [40,41] and the conductor-like polarizable continuum model (cpcm, $\varepsilon = 4$) [42], as suggested to account for the hydrophobic protein environment [43]. Optimizations were followed by calculation of the *g* tensors and hf coupling values. A frequency calculation was carried out to ensure that the computed geometry constitutes an energetic minimum. The dipeptide Ac-Tyr-NHMe was chosen as a model system in order to avoid possible truncation effects and to allow enforcement of the sidechain orientation encountered in the protein solid-state structure. For this purpose, the dihedral angles defining the backbone orientation were constrained during geometry optimization to the values from pdb 1mxr (C-N_{Tyr}-$C_{\alpha,Tyr}$-C_{Tyr}: −66.3°, N_{Tyr}-$C_{\alpha,Tyr}$-C_{Tyr}-N: −36.1°) [44], while the dihedrals describing the side chain orientation were adjusted to the values derived in a single-crystal ENDOR study (C_{Tyr}-$C_{\alpha,Tyr}$-$C_{\beta,Tyr}$-$C_{\gamma,Tyr}$: 169.4°, $C_{\alpha,Tyr}$-$C_{\beta,Tyr}$-$C_{\gamma,Tyr}$-C_{Ring}: 126.2°) [44]. No constraints were employed on any bond lengths or angles.

2.1. 263 GHz/9.4 T ENDOR spectrometer

All 263 GHz measurements were performed on a prototype ELEXSYS E780 spectrometer (Bruker BioSpin). The performance of the commercial EPR spectrometer in recording pulse EPR/PELDOR/RIDME/EDMR spectra has been reported in previous publications [45–50]. For ENDOR, the spectrometer is equipped with a cylindrical EPR/ENDOR resonator (E9501510/Bruker BioSpin) and an RF generating pulse unit. The spectrometer layout is illustrated in Fig. 1A. The bridge consists of two parts, (1) the intermediate-frequency (IF) pulse forming bridge, which operates at X-band frequencies (9.65 ± 0.4 GHz), and (2) the quasi-optical front-end converting the IF first to Ka-band (32.9 ± 0.25 GHz) and then via multiplication up to 263.3 ± 2 GHz. Our instrument is equipped with a recently installed 100 mW Amplifier-Multiplier-Chain (AMC, Virginia Diodes Inc.), which is coupled to the resonator via a corrugated waveguide. The power incident to the resonator was measured with a power meter (Virginia Diodes Inc./Erickson PM4) to be around 50 mW.

The ENDOR resonator is designed to operate in a TE_{012} cylindrical microwave mode (Fig. 1B). The frequency tuning is provided by a quartz rod (0.4/0.55 mm ID/OD) being inserted into the resonator with a fine tuning mechanism and sliding axially over the sample tube (0.2/0.33 mm ID/OD). The microwave mode is shortened by two silver plungers fixed axially in a metallic (3 mm OD/1.2 mm ID) cylinder. In addition, a fine mechanism is implemented to allow coupling adjustment during the measurements. With the available mw power and under optimal coupling, the ENDOR probe head provides mw π/2 pulses as short as 30–34 ns depending on sample and temperature (Fig. S1). The EPR pulse sensitivity was experimentally determined by measuring a single-shot echo signal from 50 μM and 10 μM ^{14}N-TEMPO in H_2O:glycerol mixture (0.8:0.2) at 10 K. It was in the range of $3 \cdot 10^9$ spins/G, as reported in SI1 and Fig. S9. The estimated sensitivity is in reasonable agreement with previously reported data for HF spectrometers [30,51–53], however does not scale with mw frequency as expected ($\omega^{7/2}$) if comparing with the 94 GHz setup, which shows nearly the same absolute sensitivity ($2 \cdot 10^9$ spins/G, SI1 and Fig. S9) but with higher mw power provided by a 2 W amplifier. The bandwidth of the loaded resonator was determined by measuring Rabi nutations of the protonated BDPA sample at RT and 10 K. It was around 1.50 GHz and 1.35 GHz, which translates into the Q-values of 180 and 200 at RT and 10 K, respectively. Thus, the conversion factor *c* of the resonator (defined here as $c = B_1/P^{1/2}$) was estimated to be in the range of 12.3–12.7 $G/\sqrt{W}$ depending on temperature, which is in accordance with the reported tabulated values for several HF resonators [54].

The ENDOR coil is designed as a saddle coil [13,29,30,53,55] in a close to Helmholtz configuration. Each coil side has 3 turns of 2.5 mm diameter closely placed to the metallic cylinder of the microwave resonator. To allow for RF penetration [13], 3 slots (60 μm wide and 200 μm spaced) are cut into the resonator wall. The coil and resonator configuration were simulated with CST Studio Suite (Computer Simulation Technology) at a radio frequency of 400 MHz. The simulation considers the coil, the resonator wall, the resonator slots and the material. For the simulation one side of the coil was connected to an RF source, the other end of the coil was terminated by a 50 Ohm load. The simulation of B_2 along the sample axis shows a maximum B_2 of 0.175 $G/\sqrt{W}$ corresponding to a π-pulse of ∼60 μs with the RF Amplifier used in this study (for B_2 profile see Fig. S3).

RF is generated by a two-channel RF pulse forming unit (Bruker DICE-II) and amplified by a 125 W RF amplifier (Amplifier Research, model 125W1000) for excitation at frequencies close to 400 MHz (^{1}H Larmor frequency at 9.4 T). A 50-Ohm semi-rigid coaxial cable (type RG 214U) leads the amplified RF to the ENDOR coil (see Fig. 1). After the coil, the cable is terminated by a 50 Ohm load to match the amplifier output and the RF transmission line. No matching circuit is used in this arrangement. The achieved coupling for the RF power (defined as S_{11}-parameter, *i.e.* reflection) is close to −3 dBc within the range of ∼ 40 MHz centered at 400 MHz (Fig. S4). The efficiency of the coil and the transmission line allows reaching typical RF π-pulse lengths of 60–70 μs practically independent of the measurement temperature (Fig. S2), as determined from Rabi-nutations in resonance with the small hf couplings of ^{1}H BDPA. These numbers are considerably different from the ones reported by Blok *et al.* with a similar setup [13], however we note that these authors did not report Rabi oscillations for ^{1}H. The availability of a broadband RF circuit is indispensable to perform pulse ENDOR experiments with stochastic RF acquisition. This acquisition mode is mandatory not only to attenuate baseline distortions due to heating effects of the RF pulses [56], but also to overcome the nuclear relaxation issues related to averaging of multiple shots at the same ENDOR frequency, as we pointed out in a previous paper [57].

To acquire orientation-selected ENDOR spectra, the magnet specifications and settings are important. The persistent magnetic field around 9.4 T is provided by a cryogen-free superconducting magnet (0–12 T), equipped with an additional coil to sweep the field in the ∼ 0.3 T range. To compensate the non-linear behavior of the magnetic field during a sweep, we utilize the field-linearization routine implemented in the Bruker software, by which the magnetic field settings are corrected during the field sweep using a calibration table for a field hysteresis. This procedure is also important to set the different field values during orientation-selected ENDOR experiments. The resolution of the field control with the sweep coil is around 0.4 μT (4 mG). Field homogeneity at the resonator position is ≤10 ppm over 10 mm along the B_0 axis, which translates into ∼100 mG at a sample length of ∼1 mm.

3. Results and discussion

3.1. ^{1}H-ENDOR on protonated BDPA

To probe the ^{1}H ENDOR performance of our spectrometer, we initially recorded ENDOR spectra of the standard BDPA radical in polystyrene (Fig. 2A, top) with three pulse sequences, *i.e.* Mims-[1], Davies- [2] and cross-polarization (CP) edited ENDOR [58]. At 263 GHz, *g* anisotropy is weakly observable and the EPR line has

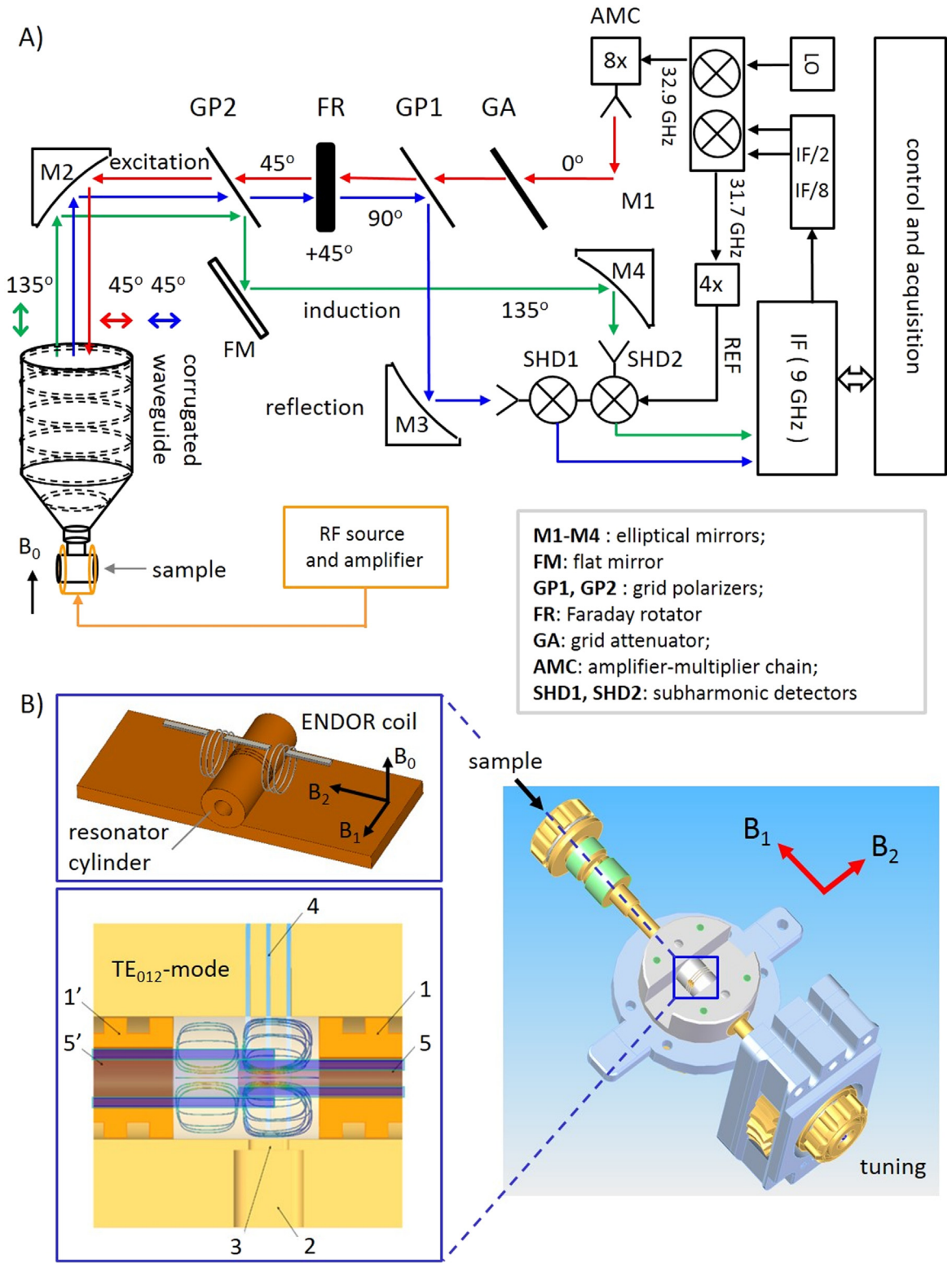

Fig. 1. (**A**) Block-scheme of the 263 GHz EPR/ENDOR spectrometer. Polarization of the incident and reflected beams is plotted in colors. After sample excitation, two detection modes are feasible: reflection and induction. With a cylindrical EPR/ENDOR resonator only the reflection mode is applicable. In the latter, the reflected signal (co-polarized to the excitation wave) is down-converted to X-band frequencies by double-mixing it with the internal reference arm (126.8 ± 0.8 GHz) for a quadrature detection. (**B**) 263 GHz EPR/ENDOR resonator and the arrangement of main working units in it. **Left (upper):** A saddle ENDOR coil mounted around the resonator and producing the RF B_2-field pointing as indicated. **Left (below):** Cavity construction and simulated B_1-field profile of the operating cylindrical TE_{012} mw mode. The figure shows the loaded resonator mode pattern. The numbered units are: *1* and *1′* – silver plungers, *2* – waveguide (0.8 mm wide), *3* – coupling iris (0.4 mm wide), *4* – slots (RF, modulation and UV access), *5* – quartz sample tube, *5′* – quartz tuning tube. For optimum pulse-EPR sensitivity, the sample extends through the entire resonator length. For pulse-ENDOR the optimum sample placement is the right half of the resonator. Three slots in a cylindrical compartment render the resonator transparent for RF and field modulation for CW EPR. Positioning of the plungers is fixed. Frequency tuning is performed with a quartz tube (*5′*) sliding within the resonator. Mechanical pre-alignment with the microwave mode, as displayed in the figure, is done during cavity assembly. The usual alignment checks are the Q-factor, the coupling strength and the nominal $\pi/2$ values for microwave (B_1) and RF (B_2) fields. **Right:** general arrangement of the plungers shown in combination with a frequency tuning mechanism.

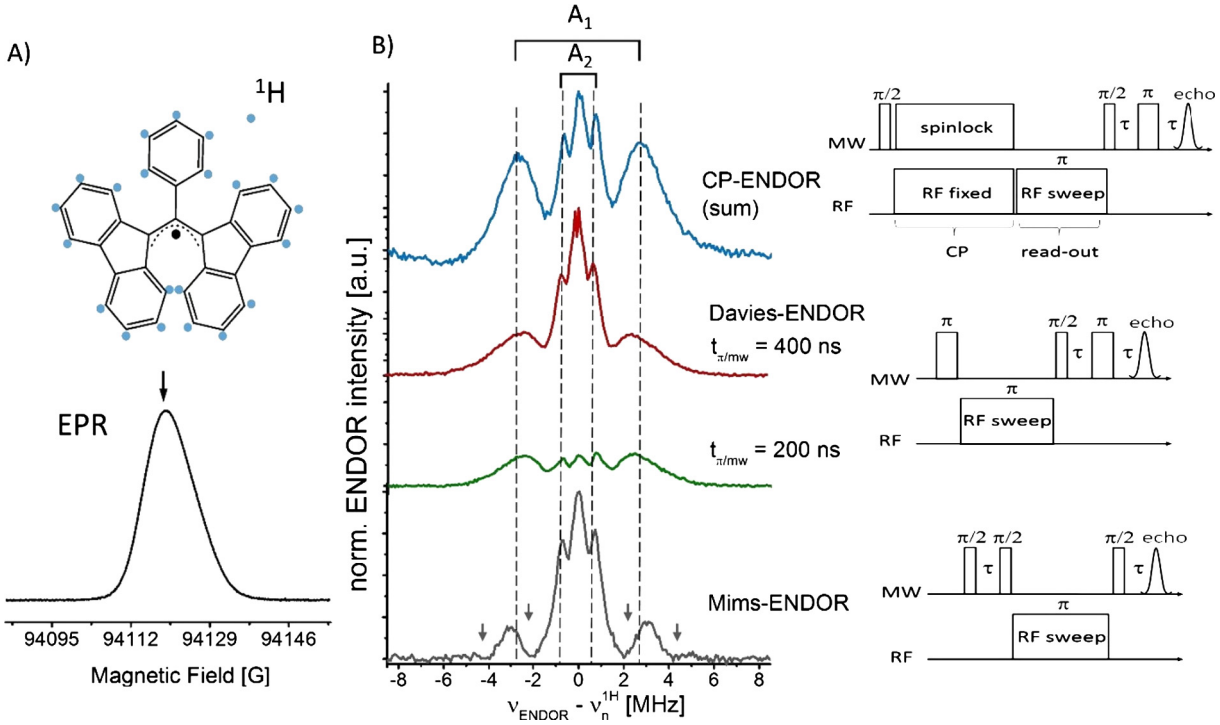

Fig. 2. (**A**) Schematic structure of the BDPA radical and 263 GHz ESE spectrum of the radical in polystyrene matrix (0.1%) at room temperature. Exp. parameters for ESE: $t_{\pi/2,mw}$ = 32 ns, SRT = 15 ms, 5 scans with 25 shots/point. (**B**) Mims-, Davies- and CP-ENDOR of protonated BDPA measured at 10 K. The expected positions of blind spots in the Mims spectrum are marked by arrows. CP-ENDOR spectrum is a sum of 26 slices, each measured varying the RF offsets $\Delta\omega_n^{CP}$ in a 2D experiment. Exp. conditions for ENDOR: T = 10 K, random RF acquisition, the total number of scans is 520; Mims: $t_{\pi/2,mw}$ = 32 ns, τ = 200 ns, $t_{\pi,RF}$ = 60 μs, SRT = 75 ms, 1 shot/point; Davies: $t_{\pi,mw}$ (inversion) = 200 ns and 400 ns; $t_{\pi/2,mw}$ (detection) = 100 ns and 200 ns, τ = 400 ns, $t_{\pi,RF}$ = 60 μs, SRT = 75 ms, 1 shot/point; CP-ENDOR: 0.48 MHz RF offset step, each slice was averaged with 20 scans and 1 shot/point, $t_{\pi/2,mw}$ = 200 ns, $\omega_{1e}/2\pi$= 1.25 MHz, t_{CP} = 200 μs, SRT = 75 ms.

a spectral width of 13 G (FWHM) due to unresolved hf splittings (Fig. 2A, bottom), offering large sensitivity for the EPR detected signal. A comparison of Davies-, Mims- and CP-ENDOR spectra is interesting, as the latter sequence is much more demanding in terms of signal stability and a successful CP-ENDOR implementation was not obvious, due to the extremely small dimensions of the resonator and the mechanical/thermal stress at helium temperature and concomitant RF irradiation. Indeed, CP-ENDOR spectra require long mw and RF irradiation (on the order of 100–200 μs) and must be acquired in a pseudo 2D fashion [59] as a function of both the applied RF frequency (ω_{RF}) and the RF offset ($\Delta\omega_n^{CP}$), (Fig. S11, SI). As CP-ENDOR spectra of individual slides are strongly asymmetric, to reconstruct a full ENDOR spectrum with true intensities, both mw and RF field strengths in the 263 GHz resonator, as well as the detected ESE signal, must be stable during the whole 2D acquisition.

For a comparison of the three experiments, spectra were recorded at 10 K with an identical total number of scans (Fig. 2B). The CP-ENDOR line shape recovered after summation of all 26 slices (Fig. S11) results symmetrically around the Larmor frequency and consistent with the line shape of the Davies ENDOR spectrum recorded with a very selective (400 ns) inversion π pulse (Fig. 2B). This observation indicates that the ENDOR double resonance structure at 263 GHz and 400 MHz maintains a stable performance over the acquisition time of this experiment, which was about 3 h at low temperature. The largest S/N was observed with the Davies sequence (400 ns preparation/inversion pulse) and was a factor of 2–3 larger than in CP- and Mims ENDOR. The result is different from our report at W-band [57], where CP-ENDOR performed favorably as compared to Davies in this temperature range. However, the effect might be rationalized by considering that the RF field strength ω_{1n} generated in the 263 GHz ENDOR resonator, which drives CP transitions, is about a factor of 3–4 lower than in our W-band resonator and that the T_{1e} is much shorter at 263 GHz than at 94 GHz (see § 3.2), disfavoring the CP experiment. The CP- and Mims ENDOR spectra show comparable S/N ratios, however the line shape in Mims ENDOR contains "blind spot" distortions not visible in CP-ENDOR. Therefore, CP-ENDOR at this frequency might be an alternative to Mims for resolving small hf couplings, however this comparison should be addressed in more details in a separate paper. A slight asymmetry between the two lines belonging to the same hf coupling is observed in all spectra but it does not correlate with a relaxation effect due to thermal polarization [60,61]. This was verified by performing Davies ENDOR experiments with increasing delay after the RF pulse [60] (Fig. S10), starting for the value employed in these sequences, *i.e.* about 1 μs. We observed that generation of asymmetry requires much longer relaxation delays. Therefore, we assign the asymmetries to a hardware effect, likely a non-linearity of the RF transmission line over the broad frequency range.

3.2. ^{1}H-ENDOR spectroscopy on a protein tyrosyl radical

3.2.1. Comparison of orientation selection at 263 GHz versus 94 GHz

When observing ENDOR spectra of organic radicals in frozen solution, such as protein radicals, the intrinsic orientation selection achieved at this high field and frequency is expected to lead to a narrowing of the ENDOR powder pattern, which corresponds to an increase in spectral resolution. However, this is the case as long as g strain does not dominate the inhomogeneous EPR line width. To examine the interplay between these two factors, we first computed the effect of orientation selection by comparing 263 GHz/9.4 T with 94 GHz/3.4 T ^{1}H ENDOR, which is the most

widespread frequency in high-field ENDOR experiments. We use the representative example of a tyrosyl radical (Y·), the most common amino acid radical encountered in biology [62]. At high fields ($\gtrsim$3 T), g anisotropy ($g_{xyz} \approx$ 2.006–2.009, 2.005, 2.002) becomes dominant in EPR for tyrosyl radicals, leading to a total spectral width of about 30–35 mT at 9.4 T, while all hf couplings are $\lesssim$ 2 mT. We first display calculated magnetization profiles $M_z(\Delta\omega)$ after rectangular π pulses of either 200 or 32 ns duration (Fig. 3). For this computation, we considered $M_z(\Delta\omega) \propto \langle S_z \rangle$ and the expression for $\langle S_z \rangle$ under the effect of a microwave pulse of amplitude $\omega_1$that fulfils the condition $\omega_1 t_p = \pi$ [15,63]:

$$\langle S_z \rangle = \frac{1}{\omega_{eff}^2}\left[(\Delta\omega)^2 + \omega_1^2 \cos(\omega_{eff} t_p)\right] \quad (1)$$

where $\omega_{eff} = \sqrt{(\Delta\omega)^2 + \omega_1^2}$ and $\Delta\omega = \omega_0 - \omega_{mw}$ is the EPR resonance offset, respectively.

To take into account the role of spectral diffusion, a hole function $f(\Delta\omega)$ has been proposed, which basically describes the envelope of Eq. (1) [3]:

$$f(\Delta\omega) = \frac{1}{\omega_{eff}^2}\left[(\Delta\omega)^2 - \omega_1^2\right] \quad (2)$$

Eq. (2) is implemented in our MATLAB routine to calculate orientation selection at high fields, as we reported in the past [30,64]. For a microwave carrier frequency ω_{mw} in resonance at $B_0 \parallel g_y$, the molecular orientations selected according to Eq. (2), and characterized by a pair of angles θ and φ (polar and azimuthal) between the

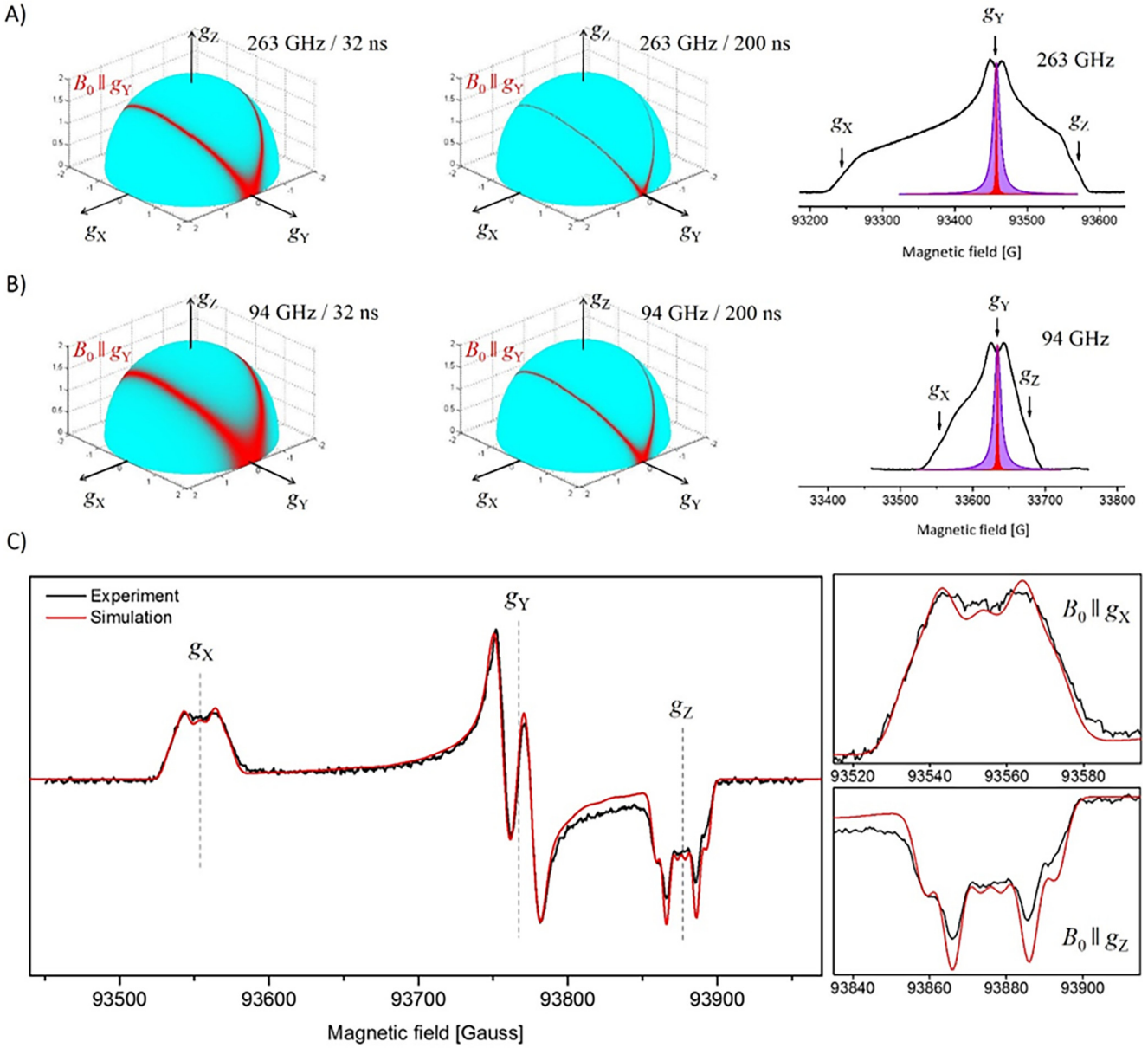

Fig. 3. (**A**, **B**) **Right:** ESE spectra of Y_{122}· at 263 GHz (**A**) vs. 94 GHz (**B**), showing the calculated excitation profiles (Eq. (2)) in the EPR line for a microwave frequency ω_{MW} in resonance at $B_0 \parallel g_y$ and a π pulse of 32 ns (magenta) and 200 ns (red), respectively. **Left** (**A** and **B**): Molecular orientations selected by these two pulse profiles are plotted on a sphere. (**C**) 263GHz echo-detected EPR spectrum (black) of Y_{122}· with simulation (red). Expansions of the g_x and g_z regions demonstrate the difference in resolution resulting from unequal g strain. Experimental conditions: c = 300 μM, in H_2O, T = 5 K, ν_{MW} = 263.078 GHz, $\pi/2$ = 100 ns, τ = 200 ns, 1024 points, 100 shots/point, 14 ms shot repetition time, 36 scans. The derivative was built after employing a Savitzky-Golay filter (4th order, 9 points). Simulation parameters: $g_{x,y,z}$ = 2.00915, 2.00460, 2.00225, Gaussian linewidth (FWHM) = 2.5 G, $g_{x,y,z}$ strain = 0.00019, 0.00011, 0.00011. All hyperfine interactions (see Table 1) included. (For interpretation of the references to colour in this figure legend, the reader is referred to the web version of this article.)

B_0 and the g tensor frame, are displayed in Fig. 3. As expected from the increased g anisotropy in the EPR spectra (about a factor of 3 from 94 to 263 GHz) the selectivity of the pulses is visibly increased at 263 GHz as compared to 94 GHz. However, the selectivity also strongly depends on the employed pulse lengths, for instance a π pulse of 200 ns at 94 GHz appears more selective than a 32 ns π pulse at 263 GHz. Therefore, optimal selectivity must be carefully evaluated for each specific experiment, for instance when comparing a Mims experiment with hard pulses vs. a Davies experiment with selective pulses.

In a second step, we evaluated the effect of g strain by simulating the 263 GHz EPR spectrum. For this, we built the first derivative of the echo-detected EPR spectrum of *E. coli* RNR $Y_{122}^{\bullet}$, as shown in Fig. 3C. As expected, the line shape is dominated by g anisotropy with additional hyperfine structure. Notably, at $B_0 \parallel g_z$ a doublet of 1:2:1 triplets is resolved arising from one large coupling to the Hβ1 nucleus as well as to the 3,5-ring protons (see Fig. 5A for ^{1}H numbering). In contrast to previous reports at 140 GHz [65], the same feature is not resolved at $B_0 \parallel g_x$, directly indicating a different inhomogeneous broadening mechanism within the EPR line. The simulation of the spectrum was consistent with a Gaussian line width (FWHM) of 2.5 G plus additional g strain of $g_{x,y,z}$ strain = 0.00019, 0.00011, 0.00011. We note that an inhomogeneous line width of ≈ 2.5 G is consistent with the hyperfine broadening provided by the other, non-resolved ^{1}H couplings (see Table 1). Therefore, at $B_0 \parallel g_z$ the line width is smaller than that previously reported at 140 GHz [65] (≈ 8 G, see SI2 and Fig. S18). Instead, the opposite trend is observed at $B_0 \parallel g_x$, where at

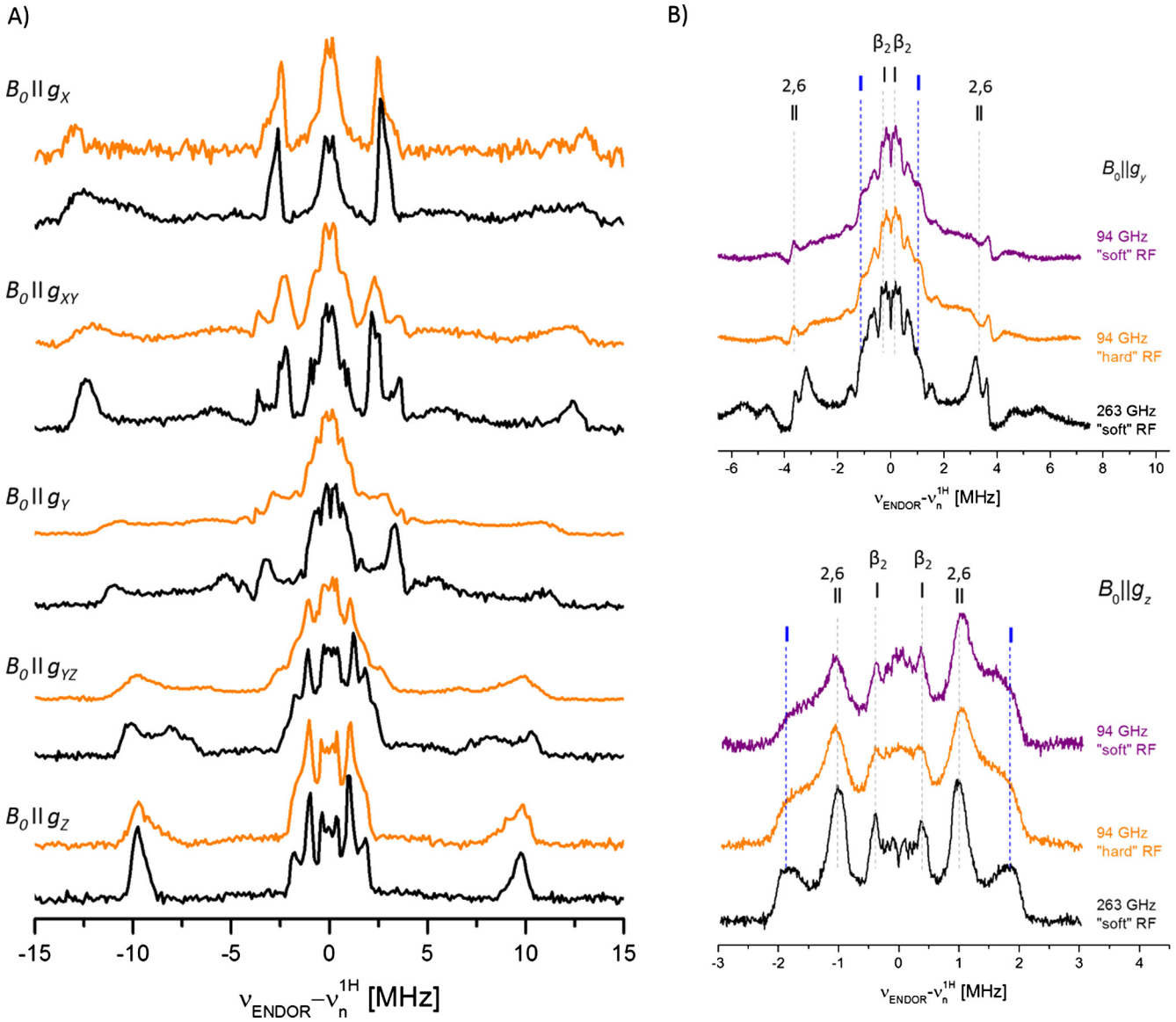

Fig. 4. (**A**) ^{1}H Davies ENDOR spectra of $Y_{122}^{\bullet}$ from *E.coli* RNR dissolved in H_2O at 263 (black) and 94 GHz (orange) recorded under comparable experimental conditions, *i.e.* $t_{\pi,mw}$ = 200 ns, $T \approx 5$–10 K, 1 shot/point, stochastic RF acquisition, 100 kHz RF resolution. Recycle delay was optimized according to the measured T_{1e} of the sample, that is ≤ 10 ms at 263 GHz vs ≈ 100 ms at 94 GHz (Table S1). Number of scans at 263 GHz was 7000–30000, number of scans at 94 GHz was 700–1500 depending on spectral position. Due to the different repetition times at 94 vs. 263 GHz, the total measurement time was comparable at both frequencies, from 6 up to 28 h depending of the spectral position. Orientations $B_0 \parallel g_x$, $B_0 \parallel g_{xy}$, $B_0 \parallel g_y$, $B_0 \parallel g_{yz}$, $B_0 \parallel g_z$ correspond to magnetic fields of 93246 G, 93346 G, 93458 G, 93515 G, 93565 G and 33436 G, 33471 G, 33510 G, 33537 G, 33555 G at frequencies 262.230 GHz and 94.045 GHz, respectively. (**B**) Spectra recorded with a higher RF resolution of 10 kHz and a "soft" RF excitation at 94 GHz for comparison. Here, the 263 GHz spectra were recorded with 19 h and 7 h acquisition time (for $B_0 \parallel g_z$ and $B_0 \parallel g_y$, respectively) as compared to 17 h and 19 h ($B_0 \parallel g_z$); and 21 h and 42 h ($B_0 \parallel g_y$) with "hard" and "soft" RT excitation at 94 GHz, respectively. Indicated assignments of the peaks are based on the previous work [30]. (For interpretation of the references to colour in this figure legend, the reader is referred to the web version of this article.)

263 GHz the line width appears dominated by *g*-strain (Fig. 3C, in red). A high-field 285 GHz EPR spectrum of Y_{122}· in *E. coli* RNR was reported also in Ref. [66]. After visual inspection, it appears to us that the same trend in line broadening is observed there as in our data. Best agreement of the simulation was achieved with g_{xyz} values of 2.00915, 2.00460 and 2.00225, with differences to the previous report [65] compatible with the error of 0.00003. Overall, the analysis of the orientation selection combined with the analysis of the EPR linewidth parameter strongly suggests that higher resolution in the orientation selected ENDOR spectra should be attainable particularly in the regions of $B_0 \parallel g_{z,y}$, where the *g* strain does not dominate the line width.

3.2.2. Comparison of spectral resolution at 263 GHz with 94 GHz

To compare resolution in ^{1}H ENDOR spectra at 263 and 94 GHz, we recorded Davies ENDOR on the same frozen protein sample from *E.coli* RNR (subunit β2) containing the stable radical Y_{122}· [67]. We note that the 263 GHz sample capillary contains about 40 times less sample volume (∼50 nL) than at 94 GHz (∼2 μL), with the sample at 263 GHz being only slightly more concentrated (300 μM vs. 200 μM at 94 GHz). Experiments at the two frequencies were conducted under corresponding optimal conditions at low temperatures. At 94 GHz, RF pulse lengths were a factor of 3 shorter and about 10 times fewer scans were required than at 263 GHz due to the larger ENDOR S/N. However, the electron spin T_{1e} relaxation at around 5–10 K was found to be much shorter at 263 GHz (Table S1), permitting a faster repetition time of the ENDOR sequence, and leading to overall similar acquisition times at both frequencies. The observation of a much shorter T_{1e} at 263 GHz is significant for EPR spectroscopy at this field, as it was found also for BDPA as well as for ^{14}N-TEMPO radical dissolved in water (Table S1) and is consistent with the trend observed in a previous report on organic radicals [68]. Although a more systematic study has to be performed, the effect is in agreement with the expectation from the so-called *direct* process [69].

Prior to a detailed analysis, we first note some general differences in the appearance of the ENDOR spectra. While most ENDOR lines become sharper at 263 GHz, the effect is particularly visible at $B_0 \parallel g_{zy}$, which is consistent with the expectations from the analysis in §3.2.1. Moreover, the enhanced resolution at $B_0 \parallel g_z$ reveals four doublets, which are not distinguishable at 94 GHz (Figs. 4 & 5). Also in a previous report at 140 GHz [30] only a total of three ^{1}H couplings were assigned at $B_0 \parallel g_z$. This excitation position has particular significance in studies of aromatic radicals [70], as here the A_z hf tensor direction of aromatic ring protons is usually parallel to the g_z direction, leading to 'single-crystal-like' line shapes of these protons. Fig. 4B illustrates 263 GHz ENDOR spectra in the region $B_0 \parallel g_{z,y}$ recorded with RF steps of 10 kHz and showing peaks as sharp as ≈ 350 kHz (at $B_0 \parallel g_z$). We note that the length of the RF pulse (60 μs) corresponds to a spectral resolution of about 16 kHz. For a better comparison, we recorded the 94 GHz spectrum also with a longer ("soft") RF pulse and 10 kHz RF steps (Fig. 4B). The spectral resolution was slightly increased but not sufficiently to resolve the doublet at ∼ ± 2 MHz at $B_0 \parallel g_z$ (Fig. 4B, marked blue). Therefore, we assign this doublet to a new ^{1}H coupling, not assigned before. The validity of the observation of the new hf coupling in the spectrum at $B_0 \parallel g_z$ will be examined in the following based on the available knowledge on the hf couplings of this particular tyrosyl radical.

3.2.3. Line shape analysis of the 263 GHz/9.4 T spectra

The DFT derived structure of the radical based on the X-ray protein structure from Ref. [44], is displayed in Fig. 5A. Previous ^{1}H ENDOR studies conducted from 9 up to 140 GHz consistently reported only six internal ^{1}H hf couplings [30,71], *i.e.* two sets of ring protons (2,6 and 3,5) in agreement with the numbering in Fig. 5) and two ^{1}H-Cβ called Hβ1 and Hβ2. We note that the ring protons might or might not be magnetically equivalent, depending on the dihedral angle (C2-C1-Cβ-Cα) between the plane of the ring (containing the C2-C1 and Cβ atoms) and the amino acid side chain orientation (defined by the plane Cβ-Cα), as pointed out previously [43,72]. For Y_{122}·, the hf couplings from the 2,6 and 3,5 ring protons were established in previous ENDOR studies and found to be pairwise magnetically equivalent [30,71]. The small Hβ2 coupling has also been assigned, however, the ^{1}H-Cα coupling has never been identified. Weak couplings (≲1 MHz) to protein residues at

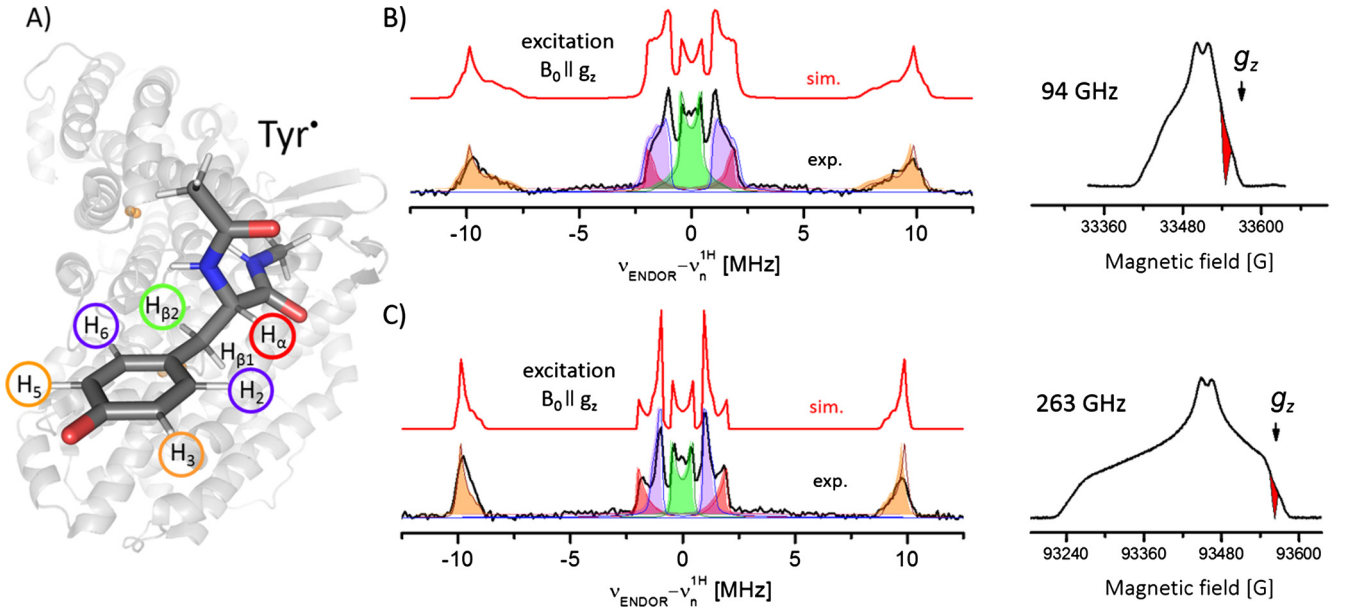

Fig. 5. (**A**) DFT optimized molecular structure of the Y_{122}· in agreement with Ref. [44] showing the numbering of the protons, which are detectable with ENDOR. 94 GHz (**B**) vs. 263 GHz (**C**) experimental (black) and simulated (red) Davies ^{1}H ENDOR spectra for $B_0 \parallel g_z$ and the corresponding ESE spectra with the indicated excitation positions. The different colors on the experimental spectra indicate the nuclei (color coding as in (**A**)) visible in the reported frequency range. (For interpretation of the references to colour in this figure legend, the reader is referred to the web version of this article.)

distances longer than typical H-bond lengths (≳2 Å) might contribute to the ^{1}H ENDOR matrix region. To rationalize the four couplings observed in the 263 GHz spectrum at $B_0 \parallel g_z$ (Fig. 5C), we first repeated 263 GHz ENDOR experiments in D_2O exchanged buffer (Fig. S12) and found that the four doublets at $B_0 \parallel g_z$ are reproducible, indicating that they must arise from internal Y· protons. Since the large Hβ1 coupling (with $A_{x,y,z} \approx 55$–59 MHz, Table 1) does not contribute to the observed ENDOR spectral region and the 2,6 as well as 3,5 protons are magnetically equivalent, respectively, the remaining couplings must originate from Hβ2 and H-Cα.

Spectral simulations were applied to examine the fidelity of the 263 GHz experiments in reporting hf tensor line shapes. For this goal, we recorded 263 GHz ENDOR spectra at five different excitation positions within the EPR line, as displayed in Figs. 5 & 6. For the simulations, we first adopted the literature values (Table 1, bold & italic entries) of six internal protons (four ring and two Hβ protons) and readjusted couplings within < 10% in order to better reproduce peaks and edges in the spectra. While the line shapes of the 3,5 ^{1}Hs are best simulated with two equivalent hf couplings (refer to Fig. S16 for simulations with inequivalent couplings), the literature values completely fail to reproduce the large peaks at ±2 MHz for $B_0 \parallel g_z$, which are resolved here for the first time. Thus, lack of resolution at lower EPR/ENDOR frequencies has led to some ambiguity in the previous assignments [30]. To gain more insight into the possible tensor form of the small ^{1}H couplings, we carried out a DFT calculation of the radical. We used a fixed conformation with a dihedral (C2-C1-Cβ-Hβ2) of 126° extracted from a single crystal EPR study [44], which was not available at the time of the 140 GHz analysis and was found consistent with high-field PELDOR data in frozen solution [64]. The conformation used for the DFT calculation is represented in Fig. 5A. We note that a more rigorous geometry optimization would require inclusion of the protein environment, which poses a great challenge due to the vicinity of a Fe_2 cluster. While this is in progress, it goes beyond the scope of the present study. Nevertheless, we employed the DFT calculation to predict the general shape and orientation of the hf tensors, particularly for the Hβ2 and H-Cα, as reported in Table 1. Because of the observed line intensities, we exclude the possibility of the new doublet arising from the 2,6 nuclei. Instead, the DFT predicts that the H-Cα couplings should be observable with the strongest component at $B_0 \parallel g_z$, while the largest component of the Hβ2 tensor should lie in the *x,y* plane, consistent with the Hβ2 bond being almost in plane with the aromatic ring [30,71]. We conclude that the new doublet at ±2 MHz observed at $B_0 \parallel g_z$ likely arises from H-Cα. We utilize this hypothesis to simulate the spectrum in Fig. 5C, which shows the consistency of this assignment with the 94 GHz experimental and simulated spectra in Fig. 5B. We assume that both Hβ2 and H-Cα tensors are characterized by one dominant component along the direction of the dipolar vector and that – for simplicity – the two other tensor components are small (≲ 1 MHz) and not distinguishable. With the Euler angles taken from the DFT calculation (Table 1), the resulting simulations for all 5 orientations are superimposed to the experimental spectra in Fig. 6 and well reproduce the subtle experimental features of the 263 GHz spectra, except small details at ≲1 MHz. The simulations were double-checked using the *EasySpin* software (Fig. S14), which led to nearly identical results. The simulation parameters are also consistent with the 94 GHz ENDOR spectra recorded at different field positions (Fig. S15).

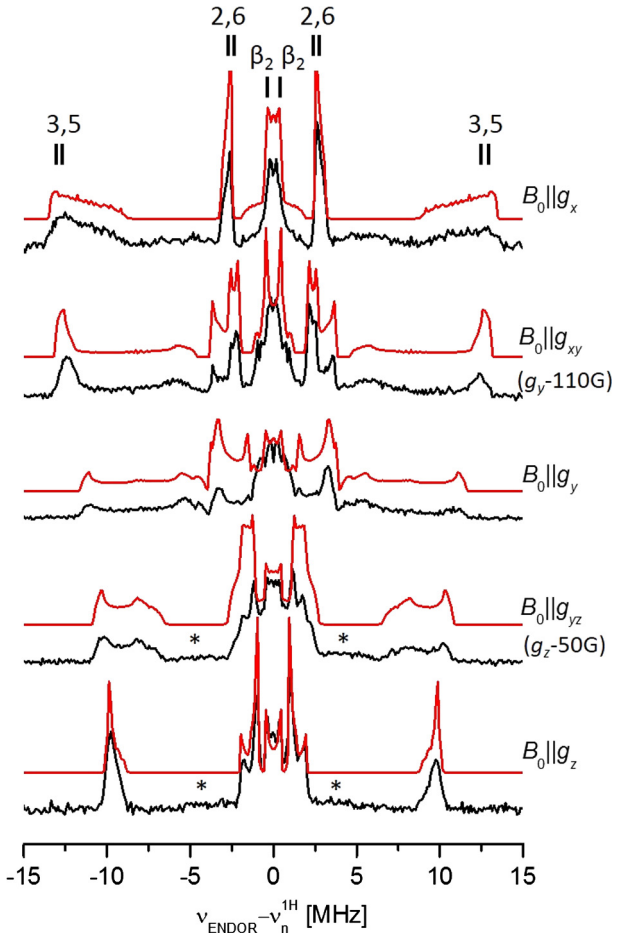

Fig. 6. Orientation selective Davies ^{1}H ENDOR for the RNR β2 protein sample in H_2O buffer. Spectra simulations (red) are overlaid for comparison and were performed for a set of seven coupled protons (see the structure in Fig. 5A) with five inequivalent hyperfine couplings (Table 1). ENDOR exp. conditions: T = 5 K, ν_{mw} = 262.2 GHz, $t_{\pi,mw}$ (inversion) = 200 ns, $t_{\pi/2,mw}$ (detection) = 100 ns, $t_{\pi,RF}$ = 60 - μs, SRT = 9 ms, 1 shot/point in stochastic acquisition, acq. time is between 6 and 28 h/spectrum, depending on the selected orientation. (For interpretation of the references to colour in this figure legend, the reader is referred to the web version of this article.)

Ultimately, precise determination of all tensor components for Hβ2 and H-Cα will require an investigation with $^2H_2$-labelled Y_{122}· combined with 263 GHz ENDOR. The feasibility to assign Hβ2 and H-Cα couplings in Y· studies at 263 GHz should deliver new structural information on Y· orientations with respect to their peptide backbone as well as provide the capability to separate internal ^{1}H couplings from external ones. We also note that the simulation does not catch broad spectral features in the range between ±3 and ±7.5 MHz (marked with stars in Fig. 6), observed also in D_2O buffer as well as at 94 GHz. Nevertheless, at the lower frequency (*i.e.* 94 GHz) these features appeared less prominent because of the broader powder pattern. These features cannot be simulated even assuming a much broader hole-function, which could be due to strong spectral diffusion. Our current hypothesis is that they arise from a lower populated radical conformation, with slightly different Hβ2 couplings. Verification of this hypothesis will require further studies with $^2H_4$-labelled Y·.

4. Conclusions

In conclusion, we have demonstrated that 263 GHz ^{1}H ENDOR can be routinely performed at low temperatures, and that long (8–12 h) signal averaging is feasible owing to the stability of a new instrumental setup. It is possible to record high-quality ^{1}H ENDOR spectra of frozen protein samples containing organic radicals at concentrations on the order of hundreds of μM in sample volumes as small as 50 nL. High-resolution ENDOR spectra of a tyrosyl radical permitted us to disentangle a new internal coupling of this important amino acid-based species. Spectral simulations,

supported by DFT calculations based on the radical structure in its active state, could reproduce all significant spectral features of the 263 GHz spectra, thus demonstrating the fidelity of the experimental setup in reporting orientation selected hyperfine tensor line shapes. High resolution combined with intrinsic high absolute sensitivity at 263 GHz will permit to expand the application of ENDOR spectroscopy to studies of more complex systems at molecular level.

Acknowledgements

We thank JoAnne Stubbe (MIT) for a previous donation of the β2 *E. coli* protein used in this study. IG, IP and PH thank all colleagues from Bruker Biospin who contributed to the project and all authors disclose no financial interest with Bruker Biospin in presenting the details of the commercial set up. This work was supported by the Max Planck Society and the Deutsche Forschungsgemeinschaft (SPP 1601).

Appendix A. Supplementary material

Supplementary data to this article can be found online at https://doi.org/10.1016/j.jmr.2019.04.001.

References

[1] W.B. Mims, Pulsed endor experiments, Proc. R. Soc. Lond. A 283 (1965) 452.
[2] E.R. Davies, A new pulse endor technique, Phys. Lett. A 47 (1974) 1–2.
[3] A. Grupp, M. Mehring, Pulsed ENDOR spectroscopy in solids, in: L. Keven, M.K. Bownam (Eds.), Modern Pulsed and Continuous-Wave Electron Spin Resonance, John Wiley and Sons, 1990.
[4] C. Gemperle, A. Schweiger, Pulsed electron-nuclear double resonance methodology, Chem. Rev. 91 (1991) 1481–1505.
[5] J.R. Harmer, Hyperfine spectroscopy – ENDOR, Emagres 5 (2016) 1493–1514.
[6] G. Feher, Observation of nuclear magnetic resonances via the electron spin resonance line, Phys. Rev. 103 (1956) 834–835.
[7] P.-P. Zänker, G. Jeschke, D. Goldfarb, Distance measurements between paramagnetic centers and a planar object by matrix Mims electron nuclear double resonance, J. Chem. Phys. 122 (2005) 024515.
[8] A.J. Pell, G. Pintacuda, C.P. Grey, Paramagnetic NMR in solution and the solid state, Prog. Nucl. Magn. Reson. Spectrosc. (2018).
[9] L. Kulik, W. Lubitz, Electron-nuclear double resonance, Photosynth. Res. 102 (2009) 391–401.
[10] O.Y. Grinberg, L.J. Berliner, Very High Frequency (VHF) ESR/EPR, Springer, Boston, MA.
[11] M. Bennati, T.F. Prisner, New developments in high field electron paramagnetic resonance with applications in structural biology, Rep. Prog. Phys. 68 (2005) 411.
[12] D. Goldfarb, High field ENDOR as a characterization tool for functional sites in microporous materials, Phys. Chem. Chem. Phys. 8 (2006) 2325–2343.
[13] H. Blok, J.A.J.M. Disselhorst, H. van der Meer, S.B. Orlinskii, J. Schmidt, ENDOR spectroscopy at 275GHz, J. Magn. Reson. 173 (2005) 49–53.
[14] A.L. Maniero, High Frequency ENDOR spectroscopy, in: O.Y. Grinberg, L.J. Berliner (Eds.), Very High Frequency (VHF) ESR/EPR, 2004, pp. 478–495.
[15] A. Schweiger, G. Jeschke, Principles of Pulse Electron Paramagnetic Resonance, Oxford University Press, New York, 2001.
[16] M. Bennati, EPR interactions – hyperfine couplings, Emagres 6 (2017) 271–281.
[17] J.M. Spaeth, I. Tkach, S. Greulich-Weber, H. Overhof, High-field optically detected EPR and ENDOR of semiconductor defects using W-band microwave Fabry-Perot resonators, Magn. Reson. Chem. 43 (2005) S153–S165.
[18] S. Kessen, C. Teutloff, J. Kern, A. Zouni, R. Bittl, High-Field 2H-Mims-ENDOR spectroscopy on PSII single crystals: hydrogen bonding of YD*, ChemPhysChem 11 (2010) 1275–1282.
[19] I. Kaminker, A. Sushenko, A. Potapov, S. Daube, B. Akabayov, I. Sagi, D. Goldfarb, Probing conformational variations at the ATPase site of the RNA helicase DbpA by high-field electron-nuclear double resonance spectroscopy, J. Am. Chem. Soc. 133 (2011) 15514–15523.
[20] T. Argirevic, C. Riplinger, J. Stubbe, F. Neese, M. Bennati, ENDOR spectroscopy and DFT calculations: evidence for the hydrogen-bond network within alpha 2 in the PCET of *E. coli* ribonucleotide reductase, J. Am. Chem. Soc. 134 (2012) 17661–17670.
[21] M. Kasanmascheff, W. Lee, T.U. Nick, J. Stubbe, M. Bennati, Radical transfer in E. coli ribonucleotide reductase: a NH2Y731/R411A-alpha mutant unmasks a new conformation of the pathway residue 731, Chem. Sci. 7 (2016) 2170–2178.
[22] B.V. Yavkin, G.V. Mamin, S.B. Orlinskii, High-frequency pulsed ENDOR spectroscopy of the NV− centre in the commercial HPHT diamond, J. Magn. Reson. 262 (2016) 15–19.
[23] P.H. Oyala, K.R. Ravichandran, M.A. Funk, P.A. Stucky, T.A. Stich, C.L. Drennan, R.D. Britt, J. Stubbe, Biophysical characterization of fluorotyrosine probes site-specifically incorporated into enzymes: *E. coli* ribonucleotide reductase as an example, J. Am. Chem. Soc. 138 (2016) 7951–7964.
[24] A. Collauto, S. Mishra, A. Litvinov, H.S. McHaourab, D. Goldfarb, Direct spectroscopic detection of ATP turnover reveals mechanistic divergence of ABC exporters, Structure (Oxford, U. K.) 25 (2017) 1264–1274.e3.
[25] A. Barwinska-Sendra, A. Basle, K.J. Waldron, S. Un, A charge polarization model for the metal-specific activity of superoxide dismutases, Phys. Chem. Chem. Phys. 20 (2018) 2363–2372.
[26] A. Nalepa, M. Malferrari, W. Lubitz, G. Venturoli, K. Moebius, A. Savitsky, Local water sensing: water exchange in bacterial photosynthetic reaction centers embedded in a trehalose glass studied using multiresonance EPR, Phys. Chem. Chem. Phys. 19 (2017) 28388–28400.
[27] J.A.J.M. Disselhorst, H. Vandermeer, O.G. Poluektov, J. Schmidt, A pulsed EPR and ENDOR spectrometer operating at 95 GHz, J. Magn. Reson., Ser A 115 (1995) 183–188.
[28] O. Burghaus, M. Rohrer, T. Gotzinger, M. Plato, K. Mobius, A novel high-field/high-frequency EPR and ENDOR spectrometer operating at 3 mm wavelength, Meas. Sci. Technol. 3 (1992) 765.
[29] M. Rohrer, M. Plato, F. Macmillan, Y. Grishin, W. Lubitz, K. Mobius, Orientation-selected 95 GHz High-Field ENDOR spectroscopy of randomly oriented plastoquinone anion radicals, J. Magn. Reson., Ser A 116 (1995) 59–66.
[30] M. Bennati, C.T. Farrar, J.A. Bryant, S.J. Inati, V. Weis, G.J. Gerfen, P. Riggs-Gelasco, J. Stubbe, R.G. Griffin, Pulsed electron-nuclear double resonance (ENDOR) at 140 GHz, J. Magn. Reson. 138 (1999) 232–243.
[31] S. Stoll, A. Schweiger, EasySpin, a comprehensive software package for spectral simulation and analysis in EPR, J. Magn. Reson. 178 (2006) 42–55.
[32] F. Neese, Wiley Interdisciplinary Reviews: Computational Molecular Science, 8 (2018) e1327.
[33] A.D. Becke, Density-functional thermochemistry. III. The role of exact exchange, J. Chem. Phys. 98 (1993) 5648–5652.
[34] C. Lee, W. Yang, R.G. Parr, Development of the Colle-Salvetti correlation-energy formula into a functional of the electron density, Phys. Rev. B 37 (1988) 785–789.
[35] S.H. Vosko, L. Wilk, M. Nusair, Accurate spin-dependent electron liquid correlation energies for local spin density calculations: a critical analysis, Can. J. Phys. 58 (1980) 1200–1211.
[36] P.J. Stephens, F.J. Devlin, C.F. Chabalowski, M.J. Frisch, Ab Initio calculation of vibrational absorption and circular dichroism spectra using density functional force fields, J. Phys. Chem. 98 (1994) 11623–11627.
[37] F. Weigend, R. Ahlrichs, Balanced basis sets of split valence, triple zeta valence and quadruple zeta valence quality for H to Rn: Design and assessment of accuracy, Phys. Chem. Chem. Phys. 7 (2005) 3297–3305.
[38] F. Neese, F. Wennmohs, A. Hansen, U. Becker, Efficient, approximate and parallel Hartree-Fock and hybrid DFT calculations. A 'chain-of-spheres' algorithm for the Hartree-Fock exchange, Chem. Phys. 356 (2009) 98–109.
[39] F. Weigend, Accurate Coulomb-fitting basis sets for H to Rn, Phys. Chem. Chem. Phys. 8 (2006) 1057–1065.
[40] S. Grimme, S. Ehrlich, L. Goerigk, Effect of the damping function in dispersion corrected density functional theory, J. Comput. Chem. 32 (2011) 1456–1465.
[41] S. Grimme, J. Antony, S. Ehrlich, H. Krieg, A consistent and accurate ab initio parametrization of density functional dispersion correction (DFT-D) for the 94 elements H-Pu, J. Chem. Phys. 132 (2010) 154104.
[42] V. Barone, M. Cossi, Quantum calculation of molecular energies and energy gradients in solution by a conductor solvent model, J. Phys. Chem. A 102 (1998) 1995–2001.
[43] S. Un, The g-values and hyperfine coupling of amino acid radicals in proteins: comparison of experimental measurements with ab initio calculations, Magn. Reson. Chem. 43 (2005) S229–S236.
[44] M. Hogbom, M. Galander, M. Andersson, M. Kolberg, W. Hofbauer, G. Lassmann, P. Nordlund, F. Lendzian, Displacement of the tyrosyl radical cofactor in ribonucleotide reductase obtained by single-crystal high-field EPR and 1.4-angstrom x-ray data, P. Natl. Acad. Sci. USA 100 (2003) 3209–3214.
[45] I. Tkach, K. Halbmair, C. Höbartner, M. Bennati, High-frequency 263 GHz PELDOR, Appl. Magn. Reson. 45 (2014) 969–979.
[46] T.U. Nick, W. Lee, S. Kassmann, F. Neese, J. Stubbe, M. Bennati, Hydrogen bond network between amino acid radical intermediates on the proton-coupled electron transfer pathway of *E. coli* alpha 2 ribonucleotide reductase, J. Am. Chem. Soc. 137 (2015) 289–298.
[47] W. Akhtar, A. Schnegg, S. Veber, C. Meier, M. Fehr, K. Lips, CW and pulsed electrically detected magnetic resonance spectroscopy at 263 GHz/12 T on operating amorphous silicon solar cells, J. Magn. Reson. 257 (2015) 94–101.
[48] D. Akhmetzyanov, H.Y.V. Ching, V. Denysenkov, P. Demay-Drouhard, H.C. Bertrand, L.C. Tabares, C. Policar, T.F. Prisner, S. Un, RIDME spectroscopy on high-spin Mn(2+) centers, Phys. Chem. Chem. Phys. 18 (2016) 30857–30866.
[49] T.U. Nick, K.R. Ravichandran, J. Stubbe, M. Kasanmascheff, M. Bennati, Spectroscopic evidence for a H bond network at Y356 located at the subunit interface of active *E. coli* ribonucleotide reductase, Biochemistry-Us 56 (2017) 3647–3656.
[50] A. Schnegg, Very-high-frequency EPR, Emagres 6 (2017) 115–131.

[51] H. Blok, J.A.J.M. Disselhorst, S.B. Orlinskii, J. Schmidt, A continuous-wave and pulsed electron spin resonance spectrometer operating at 275 GHz, J. Magn. Reson. 166 (2004) 92–99.
[52] G.W. Morley, L.C. Brunel, J. van Tol, A multifrequency high-field pulsed electron paramagnetic resonance/electron-nuclear double resonance spectrometer, Rev. Sci. Instrum. 79 (2008).
[53] M.M. Hertel, V.P. Denysenkov, M. Bennati, T.F. Prisner, Pulsed 180-GHz EPR/ENDOR/PELDOR spectroscopy, Magn. Reson. Chem. 43 (2005) S248–S255.
[54] G.M. Smith, P.A.S. Cruickshank, D.R. Bolton, D.A. Robertson, High-field pulse EPR instrumentation, Electron. Paramag. Res. 21 (2008) 216–233.
[55] I. Gromov, V. Krymov, P. Manikandan, D. Arieli, D. Goldfarb, A W-band pulsed ENDOR spectrometer: setup and application to transition metal centers, J. Magn. Reson. 139 (1999) 8–17.
[56] B. Epel, D. Arieli, D. Baute, D. Goldfarb, Improving W-band pulsed ENDOR sensitivity—random acquisition and pulsed special TRIPLE, J. Magn. Reson. 164 (2003) 78–83.
[57] R. Rizzato, M. Bennati, Enhanced sensitivity of electron-nuclear double resonance (ENDOR) by cross polarisation and relaxation, Phys. Chem. Chem. Phys. 16 (2014) 7681–7685.
[58] R. Rizzato, I. Kaminker, S. Vega, M. Bennati, Cross-polarisation edited ENDOR, Mol. Phys. 111 (2013) 2809–2823.
[59] R. Rizzato, M. Bennati, Cross-polarization electron-nuclear double resonance spectroscopy, ChemPhysChem 16 (2015) 3769–3773.
[60] M.T. Bennebroek, J. Schmidt, Pulsed ENDOR spectroscopy at large thermal spin polarizations and the absolute sign of the hyperfine interaction, J. Magn. Reson. 128 (1997) 199–206.
[61] B. Epel, A. Poppl, P. Manikandan, S. Vega, D. Goldfarb, The effect of spin relaxation on ENDOR spectra recorded at high magnetic fields and low temperatures, J. Magn. Reson. 148 (2001) 388–397.
[62] A. Migliore, N.F. Polizzi, M.J. Therien, D.N. Beratan, Biochemistry and theory of proton-coupled electron transfer, Chem. Rev. 114 (2014) 3381–3465.
[63] M. Mehring, V.A. Weberruss, Object-Oriented Magnetic Resonance, Academic Press, London, 2001.
[64] V.P. Denysenkov, T.F. Prisner, J. Stubbe, M. Bennati, High-field pulsed electron–electron double resonance spectroscopy to determine the orientation of the tyrosyl radicals in ribonucleotide reductase, Proc. Natl. Acad. Sci. 103 (2006) 13386–13390.
[65] G.J. Gerfen, B.F. Bellew, S. Un, J.M. Bollinger, J. Stubbe, R.G. Griffin, D.J. Singel, High-frequency (139.5 Ghz) Epr spectroscopy of the tyrosyl radical in *Escherichia-coli* ribonucleotide reductase, J. Am. Chem. Soc. 115 (1993) 6420–6421.
[66] S. Un, P. Dorlet, A.W. Rutherford, A high-field EPR tour of radicals in photosystems I and II, Appl. Magn. Reson. 21 (2001) 341–361.
[67] B.M. Sjöberg, P. Reichard, A. Gräslund, A. Ehrenberg, The tyrosine free radical in ribonucleotide reductase from *Escherichia coli*, J. Biol. Chem. 253 (1978) 6863–6865.
[68] L. Lumata, Z. Kovacs, A.D. Sherry, C. Malloy, S. Hill, J. van Tol, L. Yu, L. Song, M.E. Merritt, Electron spin resonance studies of trityl OX063 at a concentration optimal for DNP, Phys. Chem. Chem. Phys. 15 (2013) 9800–9807.
[69] S. Eaton, G. Eaton, Relaxation Mechanisms, in: Emagres, 2016.
[70] A. Carrington, A.D. McLachlan, Introduction to Magnetic Resonance, Harper & Row Inc, New York, 1967.
[71] C.W. Hoganson, M. Sahlin, B.M. Sjoberg, G.T. Babcock, Electron magnetic resonance of the tyrosyl radical in ribonucleotide reductase from *Escherichia coli*, J. Am. Chem. Soc. 118 (1996) 4672–4679.
[72] W. Hofbauer, A. Zouni, R. Bittl, J. Kern, P. Orth, F. Lendzian, P. Fromme, H.T. Witt, W. Lubitz, Photosystem II single crystals studied by EPR spectroscopy at 94 GHz: the tyrosine radical Y(D)(*), Proc. Natl. Acad. Sci. USA 98 (2001) 6623–6628.